fractal and fractional

Article

Load Distribution Analysis and Contact Stiffness Prediction of the Dual-Drive Ball Screw Pair Considering Guide Rail Geometric Error and Slide Position

Zhifeng Liu [1,2], Weiliang Zuo [1,3], Baobao Qi [1,3,*], Chuanhai Chen [1,3,*], Jinyan Guo [1,3], Dong Li [1,3] and Shan Gao [1,3]

[1] Key Laboratory of CNC Equipment Reliability, Ministry of Education, Jilin University,
Changchun 130025, China
[2] Institute of Advanced Manufacturing and Intelligent Technology, Beijing University of Technology,
Beijing 100124, China
[3] Key Laboratory of Advanced Manufacturing and Intelligent Technology for High-End CNC Equipment,
Changchun 130025, China
* Correspondence: qibaobao@jlu.edu.cn (B.Q.); cchchina@foxmail.com (C.C.)

Abstract: The dual-drive ball screw pair serves as a crucial element within the fixed gantry machine tool with cross-rail movement. When in service, the dual-drive ball screw pair experiences variations in axial load, impacting the contact load distribution of the ball screw pair. A calculation model for determining the axial load offset of the dual-drive ball screw pair is proposed to investigate the variation in axial load. The impact of the geometric error associated with the guide rail and the position of the slide are considered. This paper presents the contact load distribution model for the dual-drive ball screw pair. This study investigates the contact load and contact angle distribution of the dual-drive ball screw pair during the machine tool in service. Additionally, based on fractal theory, the stiffness models of individual micro-convex body and contact surfaces have been established. This study provides a comprehensive analysis of the contact stiffness of the ball screw pair, considering the influence of guide rail geometric error and slide position. In addition, the three-dimensional surface morphology of ball screw pair is obtained by experiments. This paper investigates the contact stiffness distribution of dual-drive ball screw pair during service.

Keywords: dual-drive; ball screw pair; contact load; contact angle; contact stiffness

check for updates

Citation: Liu, Z.; Zuo, W.; Qi, B.; Chen, C.; Guo, J.; Li, D.; Gao, S. Load Distribution Analysis and Contact Stiffness Prediction of the Dual-Drive Ball Screw Pair Considering Guide Rail Geometric Error and Slide Position. *Fractal Fract.* **2023**, 7, 873. https://doi.org/10.3390/fractalfract7120873

Academic Editor: Carlo Cattani

Received: 9 October 2023
Revised: 28 November 2023
Accepted: 7 December 2023
Published: 10 December 2023

1. Introduction

The ball screw pair has gained significant popularity in the precision equipment primarily due to its notable benefits, such as excellent transmission efficiency, substantial stiffness, and robust bearing capacity [1–4]. The contact load distribution and contact stiffness of a ball screw pair are critical factors influencing transmission performance [5–7]. The axial load on each ball screw pair in the dual drive system of fixed gantry machine tools with cross-rail movement is subjected to variation due to geometric error of the column guide rail and the position of the slide. And the ball contact stiffness at different positions on the screw is also different.

Every movement of the machine must take into account the dynamic interaction between the machine structure [8]. The dual-drive system of a fixed gantry machine tool with cross-rail movement exhibits motion errors that can be categorized into positioning, linear, and angle errors. The primary component influencing positioning error is the precision of the ball screw pair. In contrast, the straightness and angle errors are determined by other factors such as the surface quality of the guide rail, assembly error, and other related issues [9]. Currently, a considerable body of research focused on the modeling of geometric error in machine tool guides can be found [10–14]. Hwang et al. [15] suggested a three-probe system that can evaluate the guide rail's straightness and parallelism at the same time. Ekinci et al. [16] investigated the relationship between the motion error and the guide's geometric error. Moreover, the authors examined the internal mechanism causing the motion error. In the same year [17], an analysis was conducted to examine the relationship between the straightness and angle error. This analysis involved fitting a surface curve of a guide rail using trigonometric functions. Zha et al. [18] developed an error model to address the vertical straightness error of open hydrostatic guides. This model considers the average impact of pressure oil film error and guide rail contour error. Tang et al. [9] analyzed the characteristics of the guide rail machining process. The authors utilized measurement data to establish a systematic approach for determining the correlation between the angle and straightness error of precision linear tables and guide rail surfaces. A theoretical foundation for analyzing the axial load of the dual-drive ball screw pair under service circumstances was provided by earlier work on the modeling of the geometric inaccuracy of the guide rail.

The ball screw pair causes contact deformation due to external force, changing the ball contact load. Since the ball is in a closed raceway, it is challenging to describe the distribution of the contact load directly. Mei et al. [19] established a load distribution model considering the geometric error of the ball screw. Wei et al. [20] analyzed the contact relationship between the ball-and-screw raceway and the nut raceway. Gu et al. [21] examined the contact stiffness of ball screw pairs by employing the elastic contact theory. The authors examined the variations in the transmission stiffness of the system and the contact stiffness of the moving pair under different operational circumstances. Lin et al. [22] developed a co-ordinate system based on vector space for the ball screw. They analyzed the motion of a ball sliding and studied how contact deformation affects the resulting sliding characteristics. Based on this investigation, a kinematics model of the single-arc ball screw pair was constructed by Hu et al. [23], who also examined five different motion types at the ball contact site. Huang et al. [24] studied the normal contact load of a ball screw. The authors successfully established a correlation between normal deformation displacement and axial displacement. Feng et al. [16] proposed a lumped dynamics model to describe double-nut structures. Liu et al. [4] proposed a static analysis methodology that considers the dynamic movement of the nut. This approach can determine the load distribution on the nut at any specific place along the axis of the screw. Zhou et al. [25] proposed a novel calculating technique to determine the normal contact load between the ball and the raceway. They could not define the load condition since the study circumstance is now in a no-load state. Liu et al. [26] established a static load distribution model considering geometric errors for double-nut ball screw pairs. Zhao et al. [27] concentrated on the impact of the rotating moment caused by assembly error. However, the application of these models is not immediately practical for analyzing the contact load distribution and contact stiffness of a dual-drive ball screw pair in fixed gantry machine tools with cross-rail movement. The axial load of the dual-drive ball screw pair is subjected to variations caused by the geometric error of the guide rail and slide position. These variations impact the contact load distribution and contact stiffness of the ball screw pair.

This study introduces a calculation model for the axial force offset load of a dual-drive ball screw pair considering the guide rail geometric error and the slide position. The model considers the variable axial load of the ball screw pair during service conditions. Simultaneously, an investigation is conducted on the contact load and contact angle distribution of the ball screw during the machine tool being in service. Additionally, based on fractal theory, the contact stiffness model of the contact surface is proposed. This study provides a comprehensive analysis of the contact stiffness of the ball screw pair, considering the influence of guide rail geometric error and slide position.

2. Axial Load Offset Analysis of the Dual-Drive Ball Screw Pair

2.1. Structure Introduction of Machine Tool

The structure of the machine tool needs to be looked at to investigate how the axial load of the dual-drive ball screw pair changes in a fixed gantry machine tool with cross-rail movement. Figure 1 displays the comprehensive structure of the machine tool. The structure primarily comprises a bed, table, column, bridge, cross-rail, and slide.

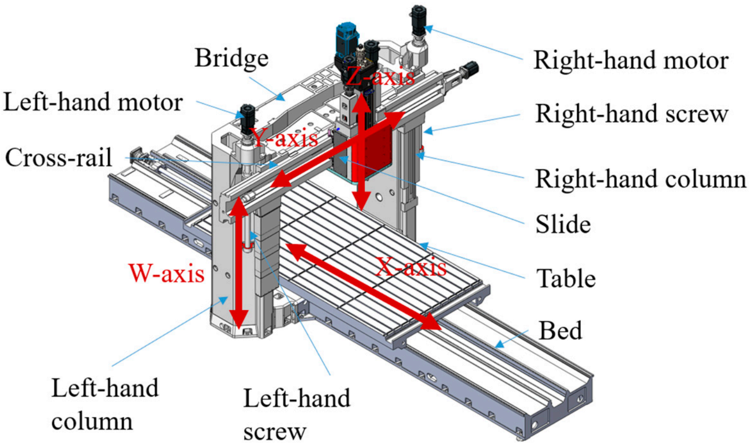

Figure 1. Fixed gantry machine structure with cross-rail movement.

2.2. Mapping Relationship between Guide Tolerance and Geometric Error

Every moving component of the machine tool has six degrees of freedom in a Cartesian co-ordinate system based on a rigid body motion co-ordinate system, under the standard BS ISO 230-1-2012 [28]. Errors occur during the movement of parts due to parallelism and straightness errors in the guide, as shown in Figure 2. If the w-axis guide rail of the machine tool is used as a case study, six geometric errors arise when the cross-rail traverses along the w-axis. These errors encompass positioning error, X-direction straightness error, Y-direction straightness error, roll error, pitch error, and yaw error (Figure 3).

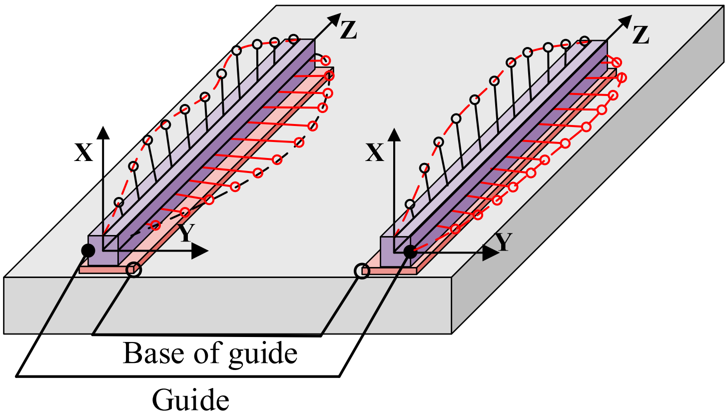

Figure 2. Guideway error diagram.

The surface topography of the components satisfies Dirichlet boundary conditions [17]. Therefore, the truncated Fourier series can describe the surface topography of the guide. The corresponding expression is as follows:

$$T(x) = \frac{k}{2} \sin\left(\frac{2\pi x}{\lambda}\right) \quad (1)$$

where $T(x)$ is the surface topography curve of the guide rail on a plane and simultaneously an amplitude. k is the straightness error of the guide. λ is the wavelength of the curve $T(x)$.

The correlation between guide tolerance and geometric error will be represented as follows:

$$\delta_Z(w) = H(w) \quad (2)$$

$$\delta_X(w) = \frac{T_X(w_{i-1}) + T_X(w_{i+1})}{2} \tag{3}$$

$$\delta_Y(w) = \frac{T_Y(w_{i-1}) + T_Y(w_{i+1})}{2} \tag{4}$$

$$\varepsilon_Z(w) = \frac{T_X(w_{i-1}) + T_X(w_{i+1})}{2L} \tag{5}$$

$$\varepsilon_X(w) = \frac{T_X(w_{i+1}) - T_X(w_{i-1})}{D} \tag{6}$$

$$\varepsilon_Y(w) = \frac{T_Y(w_{i+1}) - T_Y(w_{i-1})}{D} \tag{7}$$

where $H(w)$ is the screw error, $T_X(w)$ is the guide rail surface topography curve in X-direction. $T_Y(w)$ is the guide rail surface topography curve in Y-direction. L is the distance between the guide base of the left and right column. D is the width of the cross-rail. $\delta_Z(w)$ is positioning error. $\delta_X(w)$ is X-direction straightness. $\delta_Y(w)$ is Y-direction straightness. $\varepsilon_Z(w)$ is roll error. $\varepsilon_X(w)$ is pitch error. $\varepsilon_Y(w)$ is yaw error.

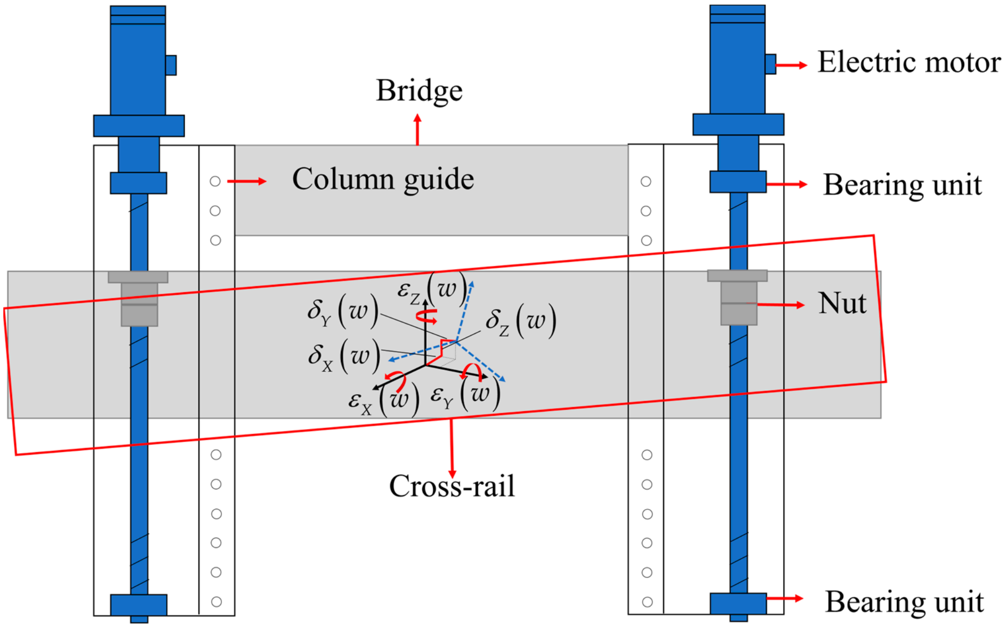

Figure 3. Structure diagram of dual-drive.

2.3. Offset Analysis of Dual-Drive Ball Screw Pair

The guide rail geometric error changes the dual-drive ball screw pair axial load when the cross-rail moves. As shown in Figure 3, the red wireframe within the illustration denotes the actual position of the cross-rail. The motor, ball screw pair, and bearing performance parameters on the left and right columns are the same, so $\delta_Z(w)$ has no effect on the center of gravity of the cross-rail. $\delta_X(w)$, $\varepsilon_Z(w)$, and $\varepsilon_Y(w)$ do not alter the cross-rail Y-Z plane center of gravity shift. And $\varepsilon_X(w)$ is determined by $\delta_Y(w)$. Therefore, the expression for the offset δ_D of the center of gravity of the cross-rail can be expressed as follows:

$$\delta_D = \delta_Y(w) \tag{8}$$

Subsequently, determining the axial loads on the dual-drive ball screw pair are conducted by considering the offset of the cross-rail center of gravity.

$$F_R^D = \frac{G_D(L_D - 2\delta_D)}{2L_D} \tag{9}$$

$$F_L^D = G_D - F_R^D \tag{10}$$

where F_L^D and F_R^D are the axial loads on the dual-drive ball screw pair when only the weight of the cross-rail is considered. G_D is the weight of the cross-rail. L_D is the distance between the dual-drive ball screw pair.

The movement of the slide along the cross-rail shifts the slide's center of gravity, altering the axial load experienced by the dual-drive ball screw pair. The axial loads on the dual-drive ball screw pair during the slide's movement can be expressed as follows:

$$F_R^H = \frac{G_H L_H}{L_D} \tag{11}$$

$$F_L^H = G_H - F_L^H \tag{12}$$

where F_L^H and F_R^H are the axial loads of the dual-drive ball screw pair when only the weight of the slide is considered. L_H is the distance between the center of gravity of the slide and the left lead screw of the dual-drive.

When the machine tool is in service, the axial loads on the dual-drive ball screw pair are expressed as follows:

$$F_R = F_R^D + F_R^H \tag{13}$$

$$F_L = F_L^D + F_L^H \tag{14}$$

3. Contact Load Distribution Modeling and Verification Analysis

The following assumptions are presented in this study for building the mechanical model of the ball screw pair.

Assumption 1. *This analysis solely considers the ball screw pair low-speed operating circumstances, ignoring the impacts of friction and sliding.*

Assumption 2. *The change in the lead screw section is not considered.*

Assumption 3. *The deformation of each contact point is limited to the elastic range. The center of curvature of the raceway aligns with the center of curvature of the ball [29,30].*

Only one of the left and right ball screw pairs in the dual-drive can be analyzed due to their identical structural makeup. Hence, the right ball screw pair is analyzed. Figure 3 shows the primary configuration of the ball screw pair. The ball screw pair is connected to the motor, while a diagonal contact bearing on the motor side restricts the screw axis and radial movement. The lower section of the screw is upheld by a radial bearing, allowing axial motion to accommodate heat expansion. When the ball screw pair is not subjected to an external load, the contact force Q_i and contact angle α_i of the ith ball and raceway are equal, respectively, $Q_{si} = Q_{ni}$ and $\alpha_{si} = \alpha_{ni}$.

3.1. Axial Deformation of Ball Screw during Movement

Figure 4 shows the axial load balance of the screw subjected to strain and compression of the nut. When the ball screw pair is in force balance, the sum of the projection of the ball contact force on the screw axis is equal to the axial external force of the ball screw pair.

The relationship between the ball contact force Q_i and the overall axial force F_a of the lead screw can be expressed as follows [19]:

$$F_a = \sum_{i=1}^{z} Q_i \sin \alpha_i \cos \lambda \tag{15}$$

where z is the number of balls. i is the ball number of the ball. α is the contact angle. λ is the pitch angle of the ball screw.

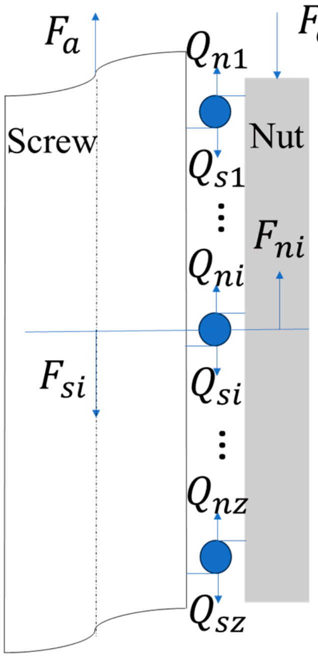

Figure 4. Balance relationship between the axial load of the ball screw pair.

The F_{si} (axial internal force) between any two ball contact points on the screw is obtained as follows:

$$F_{si} = \begin{cases} \sum\limits_{j=i+1}^{Z} Q_j \sin \alpha_j \cos \lambda, & i = 1, 2, \cdots, Z-1 \\ 0, & i = Z \end{cases} \tag{16}$$

Similarly, the F_{ni} (axial internal force) between any two ball contact points on the nut is also expressed:

$$F_{ni} = \sum_{j=i}^{Z} Q_j \sin \alpha_j \cos \lambda, \ i = 1, 2, \cdots, Z \tag{17}$$

The axial deformation between the adjacent contact points on the screw and the nut can be expressed as follows:

$$\Delta_{\zeta i} = \frac{\Delta L F_{\zeta i}}{E_\zeta S_\zeta}, \zeta = s, n \tag{18}$$

where $\zeta = s$ and $\zeta = n$ represent the screw groove and the nut groove, respectively. $E_\varsigma = (E_s, E_n)$ is the elastic modulus for the screw groove/the nut groove. ΔL is the axial distance between the contact sites of adjoining balls. $S_\zeta = (S_n, S_s)$ is the corresponding cross-sectional area for the screw groove/the nut groove.

The axial deformation relationship between the adjacent contact points on the screw and nut can be expressed as follows:

$$\varepsilon_i - \varepsilon_{i-1} = \Delta_{si} + \Delta_{ni} \tag{19}$$

where ε is the center axial displacement of the screw groove to the nut groove.

3.2. Relation between Contact Angle and Elastic Deformation

Before loading, the original contact angle of the ball contact with the screw/nut raceway is 45°. Figure 5 shows the geometric relationship between the screw and nut groove centers. The center of the ith ball, the screw, and the nut groove are denoted as O_{bi}, O_{si}, and O_{ni}, respectively. Before loading, the axial and radial lengths between the groove centers could be represented as follows:

$$C_0 = A_0 \sin \alpha_0 \tag{20}$$

$$B_0 = A_0 \cos \alpha_0 \tag{21}$$

where α_0 is the contact angle under no load. A_0 is the original space between the centers of the groove centers, which may be represented as follows:

$$A_0 = R_s + R_n - 2R_b \tag{22}$$

where R_s is the measurement of the screw groove's radius. R_b is the measurement of the nut groove's radius. R_b is the measurement of the ball's radius.

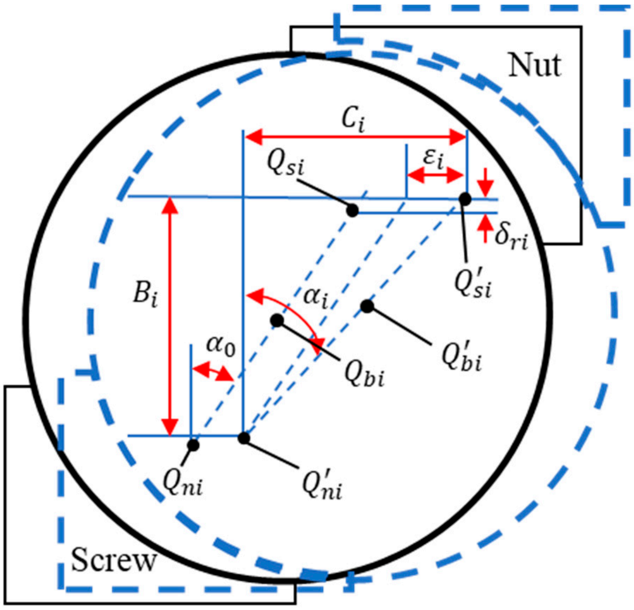

Figure 5. Geometric relationship of groove center.

A minor displacement of the screw/nut groove center and ball center will occur due to the elastic deformation of the ball screw pair following loading. Considering the influence of axial and lateral elastic deformation, the ball center and the groove center of the screw and nut are moved from O_{bi}, O_{si}, and O_{ni} to O'_{bi}, O'_{si}, and O'_{ni}. According to the geometric relationship in Figure 5, the axial distance and radial distance of the groove center after loading can be expressed as follows:

$$C_i = C_0 + \varepsilon_i \tag{23}$$

$$B_i = B_0 + \delta_{ri} \tag{24}$$

Based on the geometric relationship shown in Figure 5, the ball screw contact angle may be defined using the following equation:

$$\sin\alpha_i = \frac{C_i}{\sqrt{C_i^2 + B_i^2}} \tag{25}$$

3.3. Homogeneous Co-Ordinate Transformation

Various co-ordinate systems are constructed to assist the examination of contact load distribution in a ball screw pair, as shown in Figure 6. The global co-ordinate system $CS\begin{pmatrix} x & y & z \end{pmatrix}$ is established, the z-axis is rejoined with the screw axis, the original O is fixed in space, and the screw axis rotates at the same speed. The origin O is located in the geometric center of the angular contact ball bearing. The point p represents the projection of the center of the sphere onto the $x - y$ plane. The angle θ from the x-axis is on the line connecting the projection point p and the center point O.

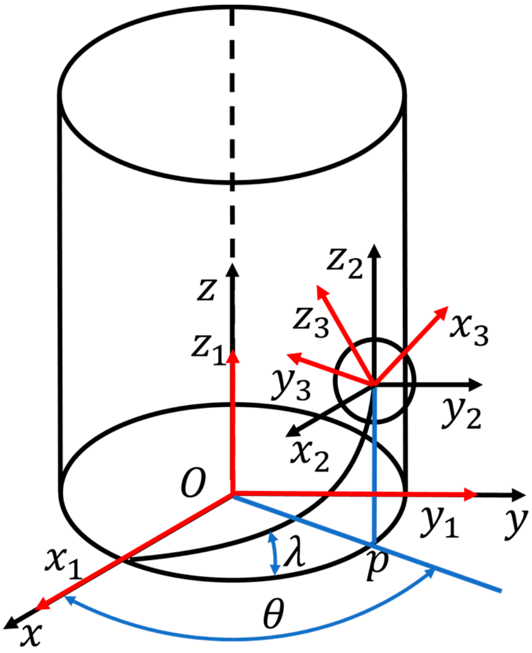

Figure 6. The spatial correlation of the co-ordinates.

The co-ordinate systems $CS\begin{pmatrix} x_1 & y_1 & z_1 \end{pmatrix}$ and $CS2\begin{pmatrix} x_2 & y_2 & z_2 \end{pmatrix}$ parallel to the global co-ordinate system are established using the center of the ball and the center of the nut base as the origin, respectively. The transformation T_{1-2} from $CS1$ to $CS2$ can be expressed as follows:

$$T_{1-2} = \mathrm{Trants}\begin{pmatrix} R_m\cos\theta & R_m\sin\theta & R_m\theta\tan\lambda \end{pmatrix} = \begin{bmatrix} 1 & 0 & 0 & R_m\cos\theta \\ 0 & 1 & 0 & R_m\sin\theta \\ 0 & 0 & 1 & R_m\theta\tan\lambda \\ 0 & 0 & 0 & 1 \end{bmatrix} \tag{26}$$

where R_m is the pitch radius of the ball screw. The parameter λ can be expressed as follows:

$$\lambda = \tan^{-1}\left(\frac{L_p}{2\pi R_m}\right) \tag{27}$$

where L_p is the pitch of the ball screw.

A new co-ordinate system $CS3(x_3 \quad y_3 \quad z_3)$ is established at the origin of the co-ordinate system $CS2$. In $CS3$, the y_3-axis is oriented perpendicular to the screw axis, and the contact points between the ball and the screw/nut are situated in the $y_3 - z_3$ plane. The transformation T_{2-3} from $CS2$ to $CS3$ can be expressed as follows:

$$T_{2-3} = \mathrm{Rot}_z\left(\theta + \frac{\pi}{2}\right) \cdot \mathrm{Rot}_y(-\lambda) = \begin{bmatrix} -\sin\theta\cos\lambda & -\cos\theta & -\sin\theta\sin\lambda & 0 \\ \cos\theta\cos\lambda & -\sin\theta & -\cos\theta\sin\lambda & 0 \\ \sin\lambda & 0 & \cos\lambda & 0 \\ 0 & 0 & 0 & 1 \end{bmatrix} \tag{28}$$

As shown in Figure 7, The origin of $CS4(x_4 \quad y_4 \quad z_4)$ is located at contact point A. The direction of the contact force is defined along the z_4-axis. The transformation T_{3-4} from $CS3$ to $CS4$ can be expressed as follows:

$$T_{3-4} = \mathrm{Rot}_z\left(-\frac{\pi}{2}\right) \cdot \mathrm{Rot}_y\left(\frac{\pi}{2} - \alpha\right) \cdot \mathrm{Trans}\begin{pmatrix}0 & 0 & -R_b\end{pmatrix} = \begin{bmatrix} 0 & 1 & 0 & 0 \\ -\sin\alpha & 0 & -\cos\alpha & R_b\cos\alpha \\ -\cos\alpha & 0 & \sin\alpha & -R_b\sin\alpha \\ 0 & 0 & 0 & 1 \end{bmatrix} \tag{29}$$

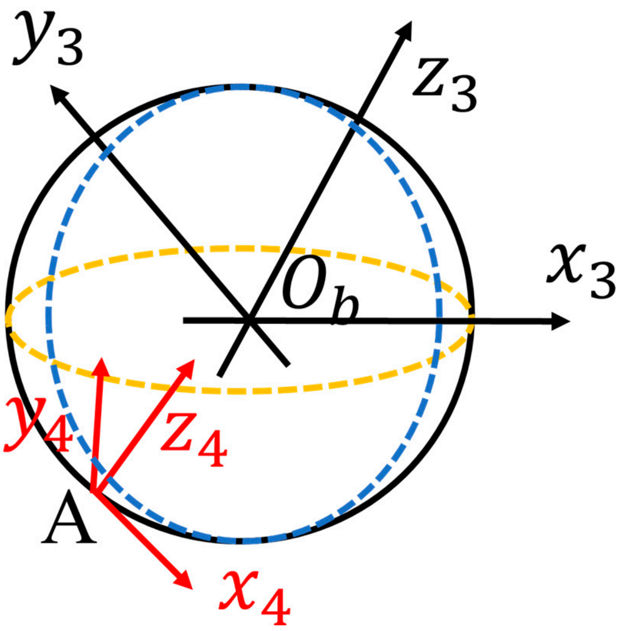

Figure 7. Co-ordinates $CS3$ and $CS4$.

When Equations (26), (28), and (29) are combined, the co-ordinate value of the contact point A in the $CS1$ can be expressed as follows:

$$\begin{bmatrix}x_A & y_A & z_A & 1\end{bmatrix}^T = T_{1-2} \cdot T_{2-3} \cdot T_{3-4} \cdot \begin{bmatrix}0 & 0 & Q_i & 1\end{bmatrix}^T \tag{30}$$

A co-ordinate system $CS5(x_5 \quad y_5 \quad z_5)$ parallel to the global co-ordinate system is established with contact point A as the origin. In the CS_5, the process of converting the contact force Q_i to its equivalent force is as follows:

$$\begin{bmatrix}Q_{xi} & Q_{yi} & Q_{zi} & 1\end{bmatrix}^T = \mathrm{Rot}_z\left(\theta + \frac{\pi}{2}\right) \cdot \mathrm{Rot}_y(-\lambda) \cdot \mathrm{Rot}_z\left(-\frac{\pi}{2}\right) \cdot \mathrm{Rot}_y\left(\frac{\pi}{2} - \alpha\right) \cdot \begin{bmatrix}0 & 0 & Q_i & 1\end{bmatrix}^T \tag{31}$$

3.4. Lateral Deformation Analysis of the Ball Screw

As shown in Figure 8, the contact force is broken down in the co-ordinate system CS_5 by assuming that the screw cross-section is rigid. The distance r_{Ai} between contact point A and screw axis is expressed as follows:

$$r_{Ai} = \sqrt{x_{Ai}^2 + y_{Ai}^2} \tag{32}$$

where x_{Ai} is the horizontal distance of the contact point A of the ith ball along the x_1-axis. y_{Ai} is the horizontal distance of the contact point A of the ith ball along the y_1-axis.

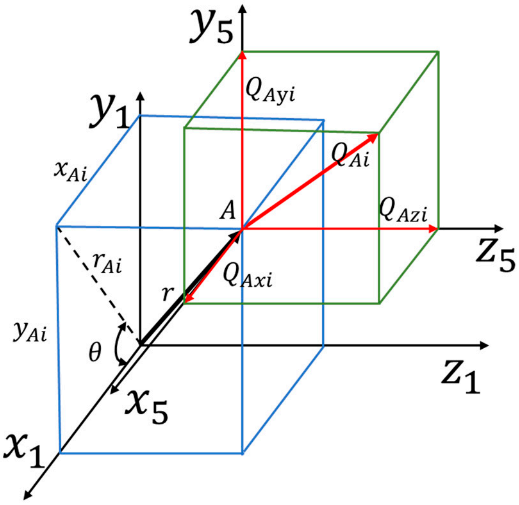

Figure 8. Projection of the contact force Q_{Ai} in the co-ordinate system CS_5.

Establishing the co-ordinate system $CS_6(x_6 \quad y_6 \quad z_6)$ parallel to the global co-ordinate system utilizes the location of the screw axis corresponding to A as the origin. Figure 9 shows the screw axis mechanical model. The addition torques T_{Axi}, T_{Ayi}, and moment M_{Ai} may be produced by the comparable shear forces Q_{Axi}, Q_{Ayi}, and axial internal force Q_{Azi} acting on the screw axis.

$$T_{Axi} = -Q_{Axi} y_{Ai} \tag{33}$$

$$T_{Ayi} = Q_{Ayi} x_{Ai} \tag{34}$$

$$M_{Ai} = Q_{Azi} r_{Ai} \tag{35}$$

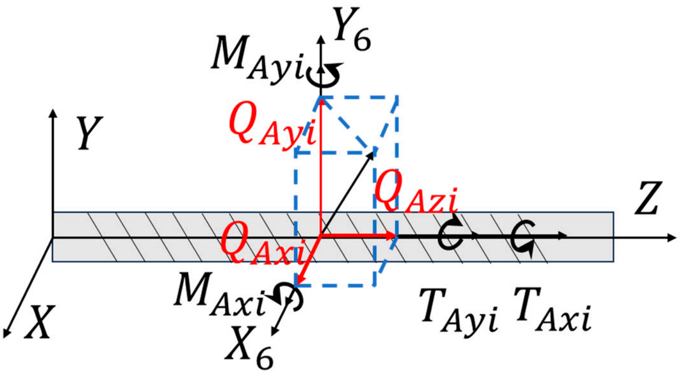

Figure 9. The addition torques T_{Axi}, T_{Ayi} and moment M_{Ai}.

The screw can be considered as a simple beam due to its significantly smaller diameter compared to its length. The mechanical examination of the screw indicates that supplementary torques T_{Axi} and T_{Ayi} do not impact the screw deformation. Screw deformation is influenced by the factors Q_{Axi}, Q_{Ayi}, Q_{Azi}, and M_{Ai}. We only consider the screw's lateral deformation caused by the forces Q_{Axi}, Q_{Ayi}, and M_{Ai} in this study. The axial deformation caused by Q_{Azi} is not considered.

The following expression can be used to represent the lateral displacement of the screw by Q_{Axi} and Q_{Ayi}:

$$w_{xi} = \sum_{j=1}^{i-1} \frac{Q_{Axj}\left(L-L_j\right)}{6EIL}\left[\frac{L}{L-L_j}\left(L_i-L_j\right)^3 + \left(L^2-\left(L-L_j\right)^2\right)L_i - L_i^3\right] + \sum_{j=i}^{z} \frac{Q_{Axj}\left(L-L_j\right)L_i}{6EIL}\left[L^2-L_i^2-\left(L-L_j\right)^2\right] \tag{36}$$

$$w_{yi} = \sum_{j=1}^{i-1} \frac{Q_{Ayj}\left(L-L_j\right)}{6EIL}\left[\frac{L}{L-L_j}\left(L_i-L_j\right)^3 + \left(L^2-\left(L-L_j\right)^2\right)L_i - L_i^3\right] + \sum_{j=i}^{z} \frac{Q_{Ayj}\left(L-L_j\right)L_i}{6EIL}\left[L^2-L_i^2-\left(L-L_j\right)^2\right] \tag{37}$$

where Q_{Axj} is the contact force along the x-axis of the jth ball at contact point A. L is the length of the screw. L_j is the distance of the jth ball from the origin O on the z-axis. E is the elastic modulus of the screw. I is the product of inertia. L_i is the distance of the ith ball from the origin O on the z-axis. Q_{Ayj} is the contact force along the y-axis of the jth ball at contact point A.

The following expression may be used to represent the lateral displacement of the screw brought on by the additional moment M_{Ai} component in the x-axis and y-axis directions:

$$w_{Mxi} = \sum_{j=1}^{i-1} \frac{M_{Aj}\cos\theta_j}{6EIL}\left[-L_i^3 + 3L\left(L_i-L_j\right)^2 + \left(L^2-3\left(L-L_j\right)^2\right)L_i\right] + \sum_{j=i}^{z} \frac{M_{Aj}\cos\theta_j L_i}{6EIL}\left[L^2-3\left(L-L_j\right)^2-L_i^2\right] \tag{38}$$

$$w_{Myi} = \sum_{j=1}^{i-1} \frac{M_{Aj}\sin\theta_j}{6EIL}\left[-L_i^3 + 3L\left(L_i-L_j\right)^2 + \left(L^2-3\left(L-L_j\right)^2\right)L_i\right] + \sum_{j=i}^{z} \frac{M_{Aj}\sin\theta_j L_i}{6EIL}\left[L^2-3\left(L-L_j\right)^2-L_i^2\right] \tag{39}$$

where M_{Aj} is the additional moment brought about by the jth ball. θ_j is the angle at which the jth ball is rotated along the screw.

The lateral deformation of the ball screw can be expressed as follows:

$$\delta_{ri} = \left(w_{xi} + w_{Mxi}\right)\cos\theta_i + \left(w_{yi} + w_{Myi}\right)\sin\theta_i \tag{40}$$

3.5. The Contact Load Modeling of the Ball Screw

The following information can be derived based on the geometric relationship shown in Figure 5:

$$\overline{O'_{si}O'_{ni}} = A_0 + \left(\delta_{si} + \delta_{ni}\right) \tag{41}$$

$$\left(\overline{O'_{si}O'_{ni}}\right)^2 = B_i^2 + C_i^2 \tag{42}$$

where, according to the Hertz contact theory, δ_{si} and δ_{ni} represent the elastic deformations of the screw and nut under the influence of the contact force:

$$\delta_{\varsigma i} = k_\varsigma Q_i^{2/3}, \varsigma = s, n \tag{43}$$

$$k_\varsigma = \frac{2K(e_\varsigma)}{\pi a_\varsigma^*}\left[\frac{9}{32}\left(\frac{1-{\mu_b}^2}{E_b} + \frac{1-{\mu_\varsigma}^2}{E_\varsigma}\right)^2 \cdot \sum\rho_\varsigma\right] \tag{44}$$

where k_ς is the Hertz contact coefficient. $K(e_\varsigma)/\pi a_\varsigma^*$ is the Hertz contact coefficient. E_b and $E_\varsigma = (E_s, E_n)$ are, respectively, the elastic modulus of the ball, the elastic modulus of the screw, and the elastic modulus of the nut. $\sum \rho_\varsigma$ is the sum of the principal curvature of the raceway at the contact point.

The axial displacement ε_i of the raceway centers relative to the ith ball can be obtained by incorporating the Equations (23), (24), (41), and (43) into Equation (42) as follows:

$$\varepsilon_i = \sqrt{\left[A_0 + (k_s + k_n) Q_i^{{}^{2}/_{3}}\right]^2 - (B_0 - \delta_{ri})^2} - C_0 \tag{45}$$

Based on the above discussion, the relationship between axial load and contact load of Equation (15) can be expressed as follows:

$$F_a = \sum_{i=1}^{z} \sqrt{\frac{\sqrt{(C_0 + \varepsilon_i)^2 + (B_0 - \delta_{ri})^2} - A_0}{k_s + k_n}}^{\,{}^{3}/_{2}} \cdot \frac{(C_0 + \varepsilon_i)}{\sqrt{(C_0 + \varepsilon_i)^2 + (B_0 - \delta_{ri})^2}} \cdot \cos\lambda \tag{46}$$

By combining Equations (13), (14), and (46), the force balance equations on the left and right ball screw pairs in the dual-drive system can be expressed as follows:

$$\begin{cases} F_L = \sum\limits_{i=1}^{z} \sqrt{\frac{\sqrt{(C_0+\varepsilon_i)^2+(B_0-\delta_{ri})^2}-A_0}{k_s+k_n}}^{\,{}^{3}/_{2}} \cdot \frac{(C_0+\varepsilon_i)}{\sqrt{(C_0+\varepsilon_i)^2+(B_0-\delta_{ri})^2}} \cdot \cos\lambda \\ F_L = G_D + G_H - \frac{G_D \cdot L_D + G_H \cdot L_H}{L} \\ F_R = \sum\limits_{i=1}^{z} \sqrt{\frac{\sqrt{(C_0+\varepsilon_i)^2+(B_0-\delta_{ri})^2}-A_0}{k_s+k_n}}^{\,{}^{3}/_{2}} \cdot \frac{(C_0+\varepsilon_i)}{\sqrt{(C_0+\varepsilon_i)^2+(B_0-\delta_{ri})^2}} \cdot \cos\lambda \\ F_R = G_D + G_H - \frac{G_D \cdot L_D + G_H \cdot L_H}{L} \end{cases} \tag{47}$$

3.6. Modeling of the Contact Stiffness Based on Fractal Theory

The contact stiffness is an important parameter that affects the dynamic performance of the contact, which is often calculated by fractal model [31]. The fractal rough surface profile is expressed by the W-M function and can be expressed as follows [32,33]:

$$z(x) = G^{(D-1)} \sum_{n=n_1}^{\infty} \gamma^{\frac{\cos 2\pi\gamma^n}{(2-D)n}}; 1 < D < 2; \gamma > 1 \tag{48}$$

where G is a scaling constant. D is the fractal dimension of the surface profile. The frequency expression denotes $\omega = \gamma^n$, and γ is related to the sampling length L_{W-M} by $\gamma^{n_1} \approx 1/L_{W-M}$, with n_1 corresponding to the low cutoff frequency of the profile. The fractal roughness parameter D, varying from 1 to 2, is dimensionless, while the scaling parameter G is not limited to a specific range and has a length dimension.

For isotropic surfaces, the relationship between the three-dimensional fractal dimension D_3 and the two-dimensional fractal dimension D is expressed as follows:

$$D_3 = D + 1 \tag{49}$$

For anisotropic surface, when any two orthogonal contours are either independent or exhibit weak correlation with each other, the three-dimensional fractal dimension D_s of the surface is expressed as follows:

$$D_s = D_{ver} + D_{hor} \tag{50}$$

where D_{ver} and D_{hor} are the dimensions of mutually orthogonal surface profiles.

The fractal parameters are determined by the logarithmic plot of the W-M power spectrum function. The power spectrum of the W-M function is expressed as follows:

$$S(w) = \frac{G^{2(D-1)}}{2\ln\gamma}\frac{1}{\omega^{(5-2D)}} \tag{51}$$

Calculating the logarithm of Equation (51), then:

$$\mathrm{lg}S(\omega) = 2(D-1)\mathrm{lg}G - \mathrm{lg}2\ln\gamma + (2D-5)\mathrm{lg}\omega \tag{52}$$

Equation (52) can be expressed as follows:

$$\mathrm{lg}S(\omega) = k\mathrm{lg}\omega + b \tag{53}$$

where $k = 2D - 5$, $b = 2(D-1)\mathrm{lg}G - \mathrm{lg}2\ln\gamma$.

Then, the fractal dimension D and the parting roughness parameter G can be expressed as follows:

$$\left.\begin{array}{l} D = \frac{(k+5)}{2} \\ \log G = \frac{b+\log(2\ln\gamma)}{2(D-1)} \end{array}\right\} \tag{54}$$

The number of micro-convex bodies with contact areas between a and $a + da$ can be expressed as follows:

$$n(a) = -\frac{dN}{da} = \frac{D}{2}\frac{a_l^{D/2}}{a^{(D/2+1)}} \tag{55}$$

For the contact between two rough surfaces, the number of micro-convex $n'(a)$ can be expressed as follows:

$$n'(a) = \lambda \cdot n(a) = \left[\frac{\left(\frac{4}{\pi E'}\frac{R_1 r_b}{R_1 - r_b}\right)^{1/2}}{\pi(R_1 - r_b)}\right]^{\left(\frac{1}{r_b} - \frac{1}{R_1}\right)} \cdot n(a) \tag{56}$$

According to fractal theory, the three stages of elastic deformation, elastoplastic deformation, and plastic deformation were analyzed separately.

When $\delta < \delta_{ec}(a > a_{ec})$, the micro-convex body is in a state of complete elastic contact. The critical elastic contact area can be expressed as follows:

$$a_{ec} = G^2\left(\frac{3E^*}{4\pi k\sigma_s}\right)^{\frac{1}{D-1}} \tag{57}$$

When in the elastoplastic contact state, the area of contact deformation can be expressed as follows:

$$a_{pc} = G\left(\frac{\beta E}{\sigma_s}\right)^{\frac{2}{D-1}} \tag{58}$$

where $\beta = \frac{\left(\frac{2m+1}{2m}\right)^{2(m-1)}\pi^{1/2}}{(30\times 0.2^{1/m})^{m/(m-1)}}$.

When $a < a_{pc}$, the contact point undergoes complete plastic deformation. The contact area can be expressed as follows:

$$a_p = 2\pi R_p \delta \tag{59}$$

where the relationship between the top radius R_p of the micro-convex body and the contact area a can be expressed as follows:

$$R_p = \frac{a^{D/2}}{2\pi G^{(D-1)}} \tag{60}$$

The normal stiffness of a single micro-convex body can be expressed as follows:

$$k_n = \frac{dF_e}{d\delta} \tag{61}$$

According to the formulas for calculating the contact force and contact deformation of the micro-convex body in references [32,33], the normal contact stiffness of the elastic stage and the normal contact stiffness of the elastoplastic stage are, respectively, expressed as follows:

$$k_{nec} = \frac{dF_{ec}}{d\delta} = \frac{4E}{3\sqrt{\pi}} \cdot \frac{3-D}{2-D} a^{1/2} \tag{62}$$

$$k_{nep} = \frac{dF_{ep}}{d\delta} = \frac{2}{3}\sigma_s^{\frac{(m-1)}{m}} \cdot \left[0.2E^* \sqrt{\pi} \left(\frac{2m+1}{2m}\right)^{2(m-1)}\right]^{\frac{1}{m}} G^{\frac{(D-1)}{m}} \cdot a^{\frac{Dm+1-D}{2m}} \cdot \frac{2}{2-D} \left[\left[2 + \ln\left(\frac{\varphi^{(1-\frac{1}{m})}}{3 \times 0.2^{1/m}}\right)\right] \cdot \frac{2m+1-D}{2m} + \frac{m - mD - 1 + D}{2m}\right] \tag{63}$$

Combining Equations (56), (62), and (63), the contact stiffness can be expressed as follows:

$$K_n = \int_{a_{ec}}^{al} k_{nec} n'(a) da + \int_{a_{pc}}^{a_{ec}} k_{nep} n'(a) da \tag{64}$$

Figure 10 illustrates the contact load distribution and contact stiffness calculation procedure for the ball screws.

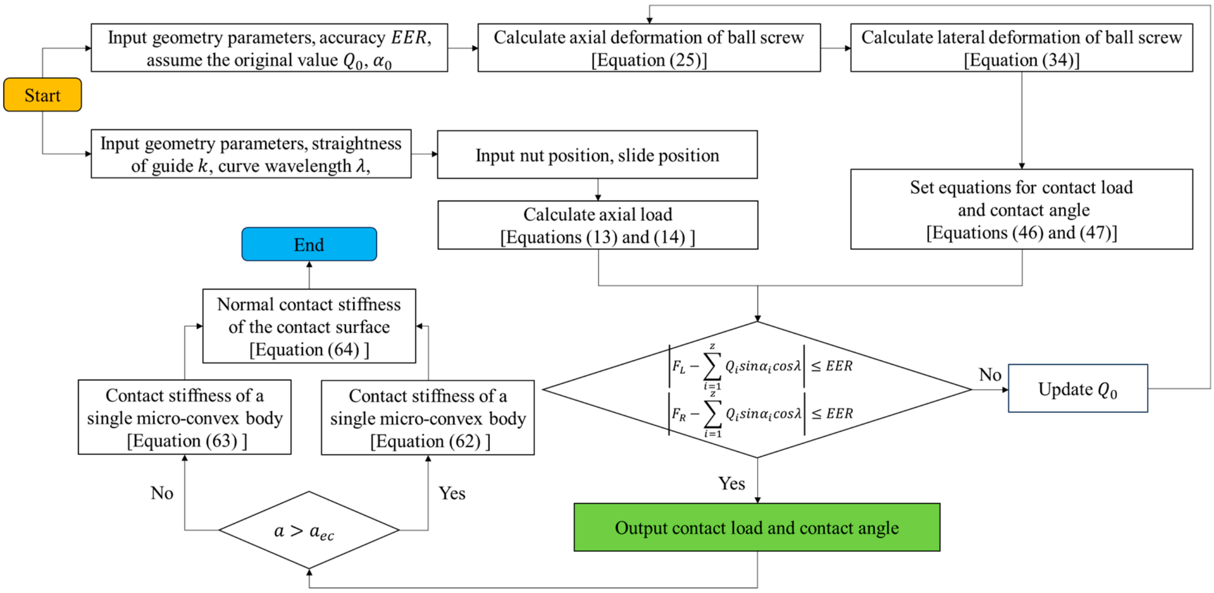

Figure 10. Flow chart.

3.7. Finite Element Verification

One company model, 6008-3 ball screw pair, is used for finite element modeling, which reduces numerical calculation and simulation calculations and verifies the force analysis model. There are 125 balls in total, with the nominal diameter being 60 mm, the lead being 8 mm, the ball diameter being 4.763 mm, and the nut outer diameter being 90 mm. Figure 11 shows the ball screw pair three-dimensional mesh. One end of the screw is fixed and the other end allows it to translate along the axis. The axial load is 5000 N. The contact is frictional and the coefficient of friction is 0.002. Figure 12 shows the stress cloud representations of the ball bearings. Figure 13 shows the distribution of contact load during the finite element analysis. The numerical analysis is considered adequate based on the evidence of a maximum error of 8.7%.

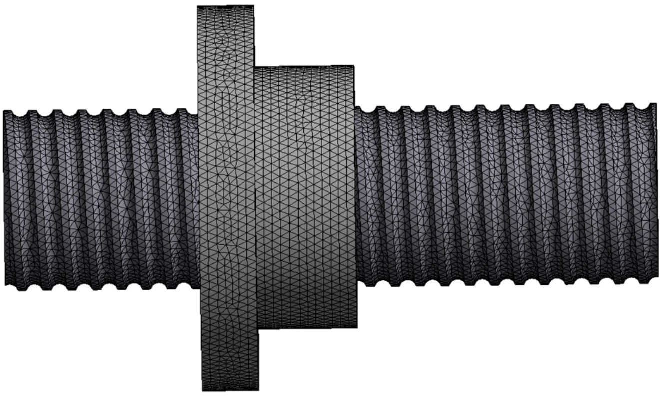

Figure 11. Three-dimensional mesh of ball screw.

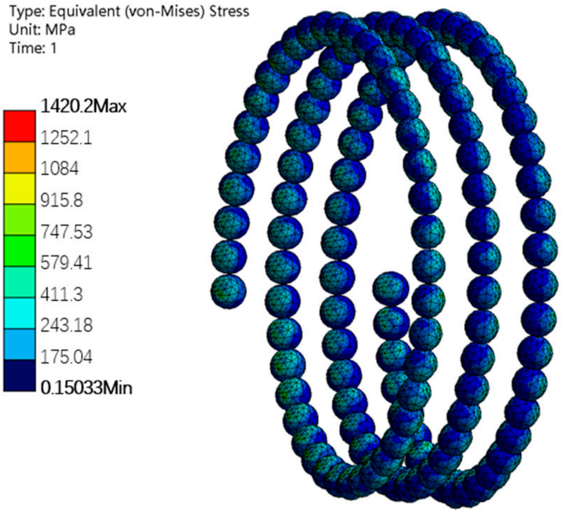

Figure 12. Stress cloud images of all ball bearings.

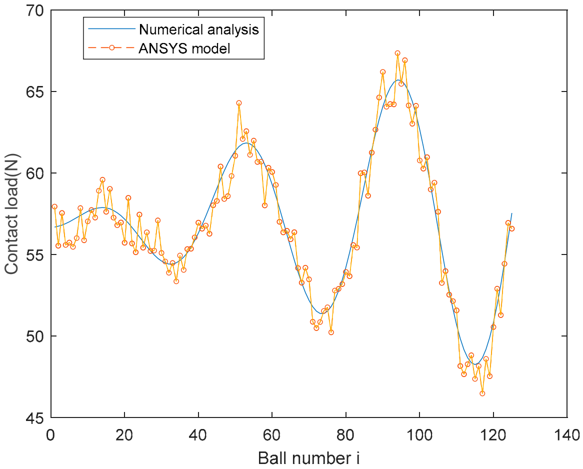

Figure 13. Comparison of the numerical analysis and finite element analysis.

4. Results and Discussion

Table 1 shows the parameters of the dual-drive ball screw pair in the fixed gantry machine with cross-rail movement.

Table 1. Ball screw parameters.

Parameters	Value	Unit
Ball radius	6.35	mm
Screw groove radius	6.985	mm
Nut groove radius	6.985	mm
Length of screw	1200	mm
Nominal pitch circle radius	50	mm
Nominal pitch	16	mm
Number of balls	380	/
Outer diameter of nut	155	mm
Length of nut	311	mm
Elastic modulus	210×10^9	Pa
Poisson ratio	0.3	/
Helix angle	2.9155	degree

4.1. Verification of the Proposed Model

The proposed model was compared to the model from [19], as shown in Figure 14. The reference [19] exclusively focuses on the axial deformation of the screw. When an axial load is applied, the deformation of the front ball is greater than that of the rear ball. Therefore, the contact load on the ball shows a decreasing trend. In the paper's model, the axial deformation of the screw, the lateral deformation of the screw, and the change in the contact angle of the ball are considered. Hence, the distribution of the contact load on the ball exhibits periodicity with an increasing amplitude.

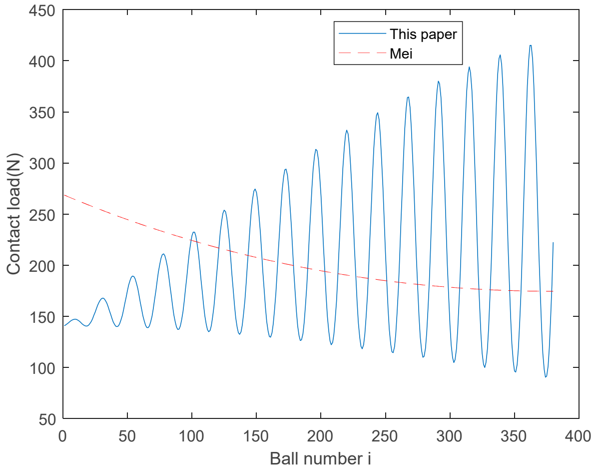

Figure 14. Comparison of contact load distribution.

4.2. Distribution Analysis of Contact Load/Angle with Ball Screw Positions

It is assumed that the ball screw pair is devoid of any preload to investigate the effect of screw elastic deformation on the ball contact angle and contact load distribution. When ignoring the impact of the guide rail geometric error and the slide position, the axial load of the dual-drive ball screw pair remains constant, assuming a value of 55 kN. The overall distribution of the contact load is shown in Figure 15. The contact load distribution can be described by a complex nonlinear behavior. When the nut is in different positions of the screw, the contact load distribution curves show different shapes. The uneven distribution of the nut under the middle screw is preferable to the nut at both ends of the screw. Because, the middle portion of the screw is more prone to deformation than the upper and lower end of the screw. When the nut is located at the upper, middle, and lower end of the screw, the standard deviation of the contact load distribution is 78.38, 30.05, and 64.98, respectively. Additionally, the average contact load value—roughly 196.17 N—remains relatively constant as the nut position with the screw varies.

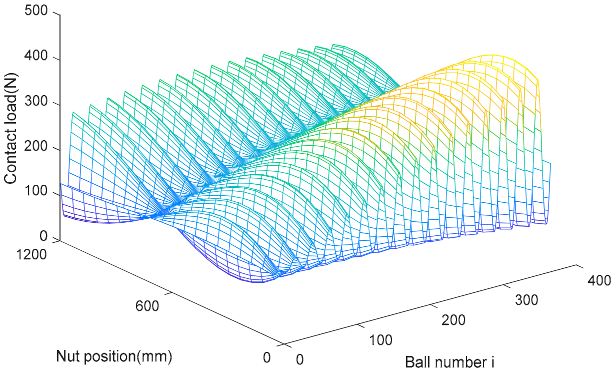

Figure 15. The phenomenon of contact load distribution.

One of the crucial ball screw parameters is the contact angle, which is distributed along the screw direction in relation to the nut position, as shown in Figure 16. It is evident that the distribution of the contact angle exhibits complex nonlinear behavior, similar to the change in contact load distribution. When the nut is located at the upper, middle, and lower end of the screw, the standard deviation of the contact angle distribution is 0.0337, 0.0130, and 0.0285, respectively. Nonetheless, there is always an opposition between the curve shapes of the contact load distribution and the contact angle.

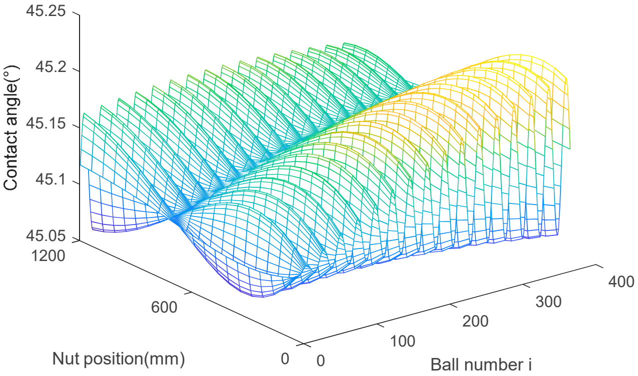

Figure 16. The phenomenon of contact angle distribution.

4.3. Distribution Analysis of Contact Load Based on Multiple Influencing Factors

Figure 17 shows the contact load distribution curve considering different axial load conditions ($F_a = 35,000\ N$, $F_a = 55,000\ N$, and $F_a = 75,000\ N$) when the nut is in the middle of the screw. The unevenness of the load distribution increases with axial load. The standard deviations of contact load distribution are 18.71, 32.74, and 37.95, respectively. However, the fluctuation period of the contact load distribution is roughly the same. Figure 18 shows the contact angle distribution curve considering different axial load conditions ($F_a = 35,000\ N$, $F_a = 55,000\ N$, and $F_a = 75,000\ N$) when the nut is in the middle of the screw. The unevenness of the contact angle distribution increases with axial load. The standard deviations of contact angle distribution are 0.0096, 0.0144, and 0.0191, respectively.

Figures 19 and 20 show the distribution phenomenon of contact load/angle under different initial contact angles ($\alpha_0 = 45°$, $\alpha_0 = 46°$, and $\alpha_0 = 47°$). The standard deviations of contact load distribution at different initial contact angles are 32.74, 32.44, and 32.17, respectively, indicating a decreasing trend. The standard deviations of the contact angle distribution under different initial contact angles are constant, which is 0.0144.

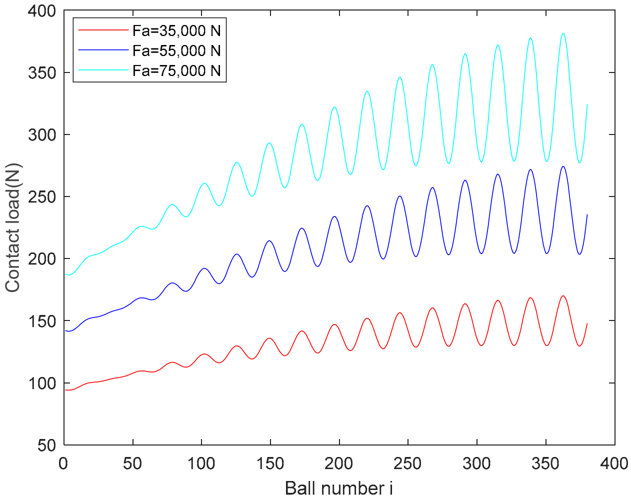

Figure 17. The influence of axial load on the contact load distribution.

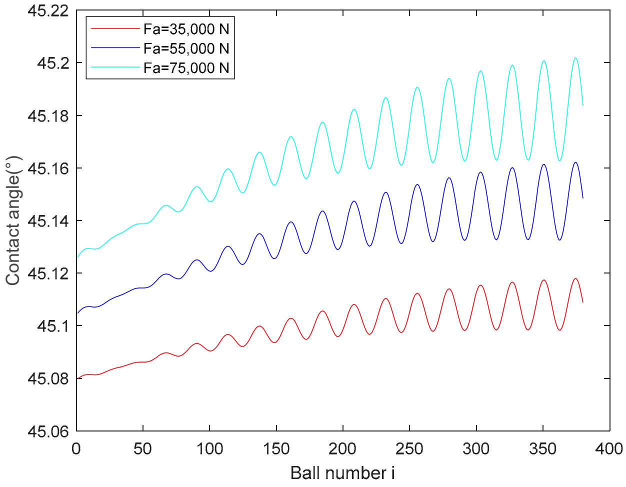

Figure 18. The influence of axial load on the contact angle distribution.

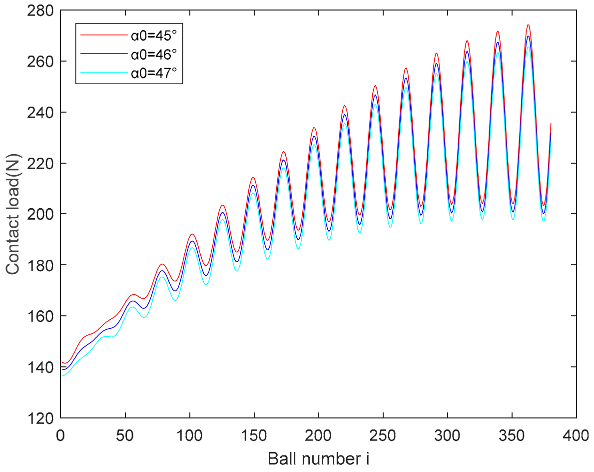

Figure 19. The influence characteristic of contact angle on the contact load.

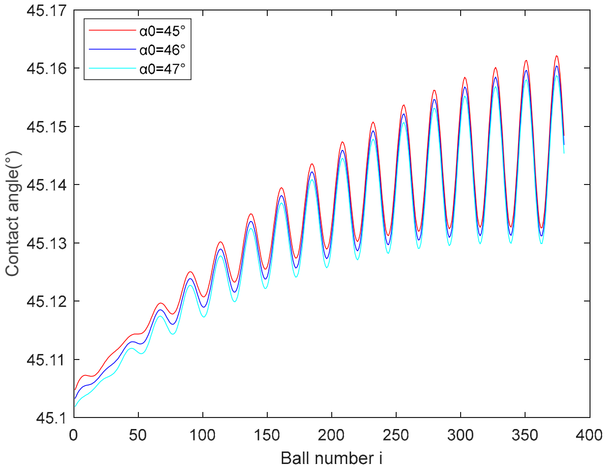

Figure 20. The evolution characteristic of the contact angle based on original contact angle.

4.4. Axial Load Change on Dual-Drive Ball Screw Pair

The machine tool has a cross-rail weight of 5000 kg, a slide weight of 6000 kg, and dual-drive ball screw pair spacing of 4410 mm. The axial loads of the dual-drive ball screw pair can be determined via Equations (13) and (14) when the machine tool is in service. The axial load of the ball screw pair on the left column during machine service has a maximum of 76,490 N and a minimum of 36,430 N, as shown in Figure 21. The ball screw pair on the right column has maximum and lowest axial loads of 78,570 N and 38,510 N, as shown in Figure 22. Due to the geometric error of the guide on the column, the maximum and minimum axial loads on the ball screw pairs on the left and right columns are different.

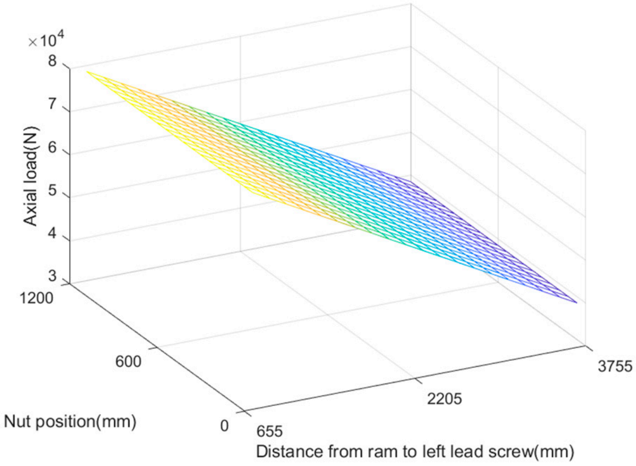

Figure 21. Axial load distribution of the ball screw pair on the left column when the machine tool is in service.

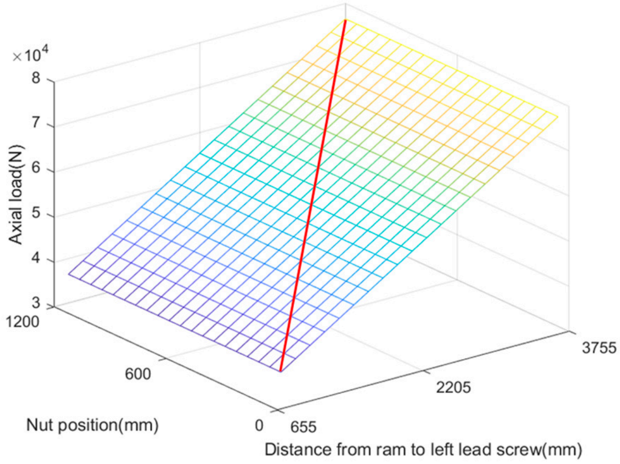

Figure 22. Axial load distribution of the ball screw pair on the right column when the machine tool is in service.

4.5. Distribution of Contact Load and Contact Angle under an Offset

Because the maximum axial load of the ball screw pair on the right column is larger than that of the ball screw pair on the left column. Therefore, this analysis focuses on the contact load and contact angle distribution of the ball screw pair located on the right column. The distribution range of the contact force is shown in Figure 23. The distribution range of the contact angle is shown in Figure 24.

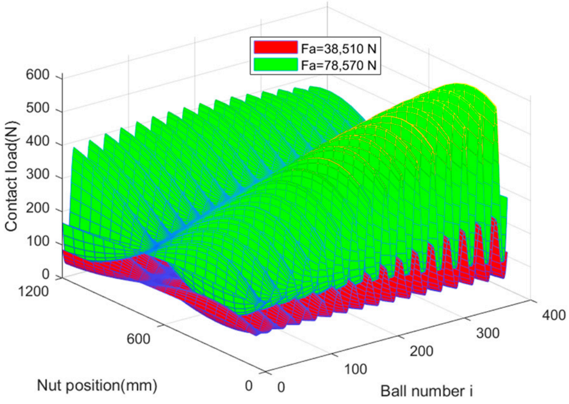

Figure 23. Distribution range of the contact load.

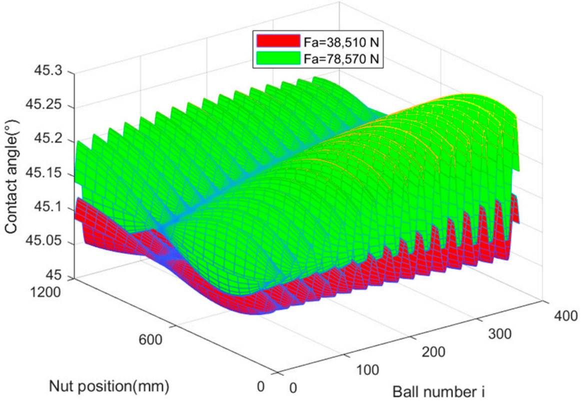

Figure 24. Distribution range of the contact angle.

When the machine tool is in service, the contact load distribution of the ball screw pair on the right column is analyzed using the axial loads and nut locations on the diagonal shown in Figure 22 (position of the red line). Figure 25 shows the contact load distribution curve. Figure 26 shows the contact angle distribution curve. Because the axial load on the nut is greater when it is located at the end of the screw, the contact load distribution and contact angle distribution are more uneven.

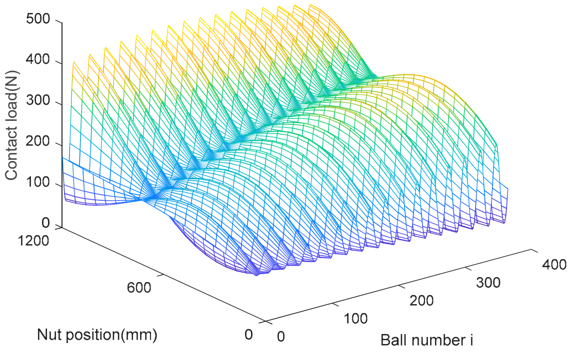

Figure 25. The phenomenon of contact load distribution under offset.

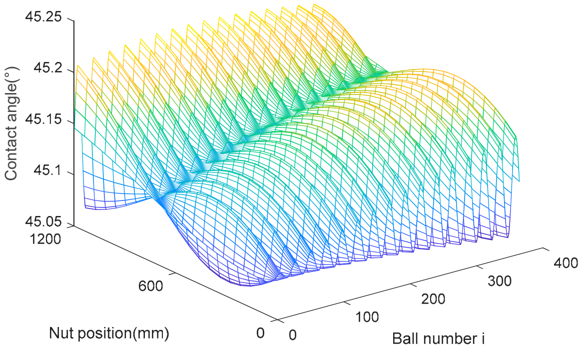

Figure 26. The phenomenon of contact angle distribution under offset.

As Figure 27 shows, there is a similar evolutionary trend between contact load and axial load, that is, increasing or decreasing simultaneously. However, due to the existence of geometric errors, the maximum contact load of the ball does not change linearly on the screw. As shown in Figure 28, the maximum contact load of the ball exhibits a trend of growing, reducing, and increasing with the change in axial load and the movement of the nut position.

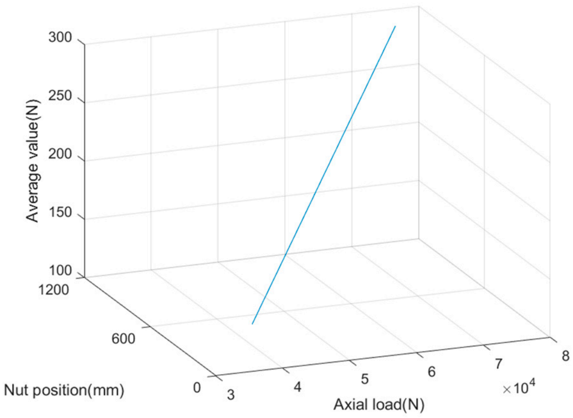

Figure 27. Mean contact load.

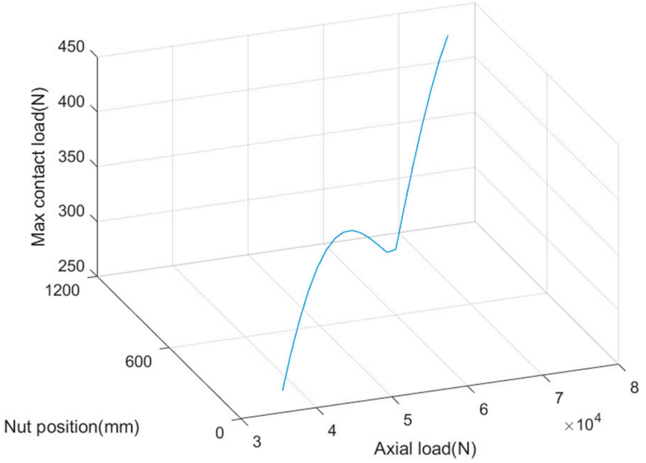

Figure 28. Maximum contact load of the ball.

4.6. Contact Stiffness Analysis of Ball Screw Pair

The comprehensive influence of G and D on K_{ne} is shown in Figure 29. It can be concluded that, when D remains constant, K_{ne} monotonically decreases with the increase in G. When parameter G is an exact value, the value of K_{ne} monotonically increases with the increase in D.

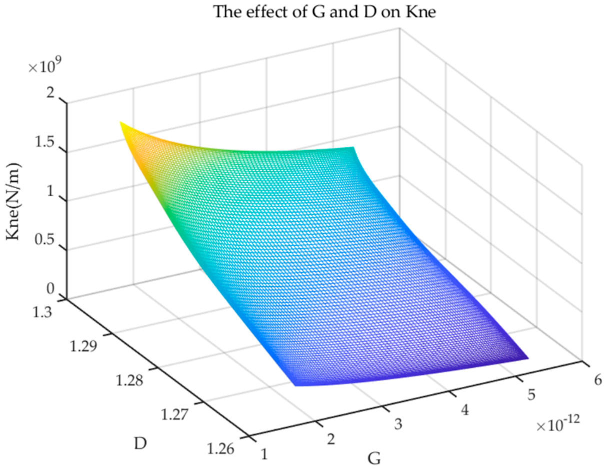

Figure 29. Comprehensive analysis of contact stiffness with G and D.

This paper uses the power spectrum density method to calculate the fractal dimension D and the fractal parameter G, and it is based on the measured surface data. As shown in Figure 30, a three-dimensional topography tester is used to measure the surface appearance of the dual-drive ball screw pair test sample of the machine tool. The surface morphology of the test sample is shown in Figure 31. Figure 32 shows the power spectral density of ball screw specimen [32]. The linear fitting function can be obtained by using the least square method. The fractal dimension D and the fractal parameter G of the ball screw specimen are 1.28 and 3.5×10^{-12}, respectively.

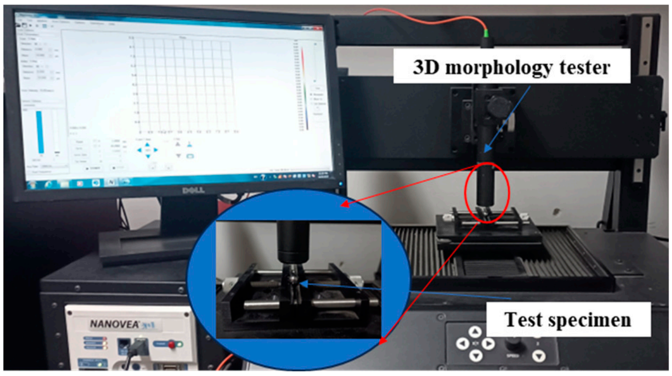

Figure 30. Three-dimensional topography scanning experiment.

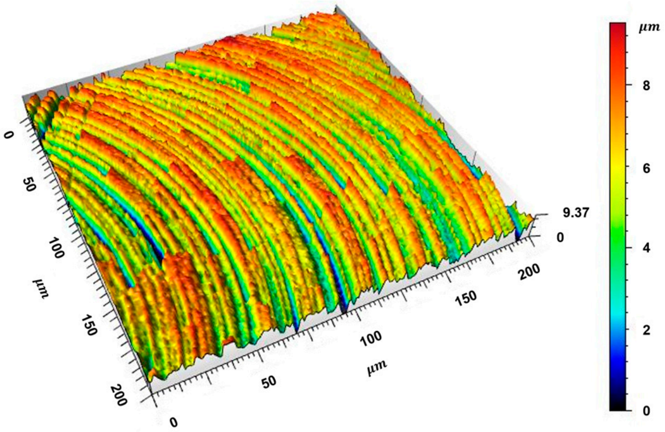

Figure 31. The surface morphology of the test sample.

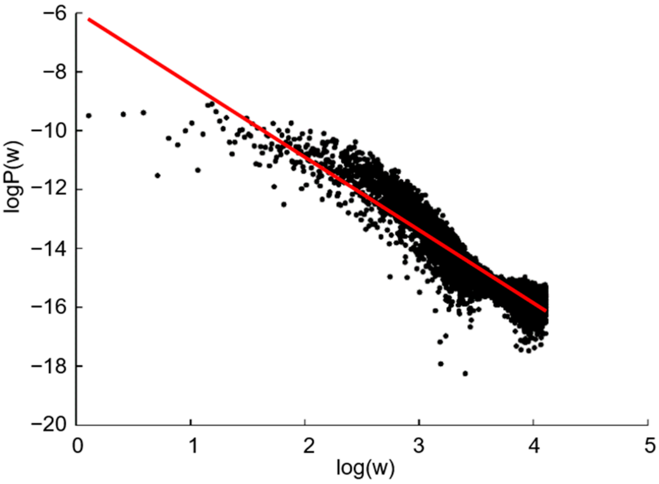

Figure 32. The power spectrum density.

The contact stiffness of the ball screw pair on the right column can be obtained by combining the test parameters with the contact load shown in Figure 25. Due to the influence of the geometric error of the guide rail and the position of the slide, the contact stiffness of the ball screw pair on the right column also presents a complex nonlinear, as shown in Figure 33.

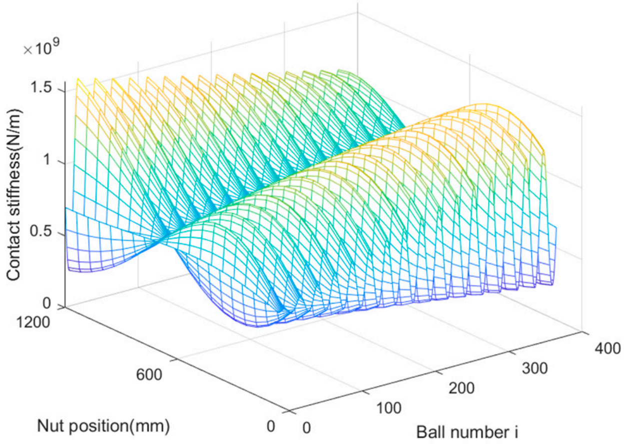

Figure 33. Contact stiffness of ball screw.

5. Conclusions

A load model of the dual-drive ball screw pair in service condition is proposed in this study by considering the influence of the guide rail geometric error and the slide position. A detailed analysis is conducted on the impact of nut position and axial load on the load distribution phenomenon. And the contact stiffness of a ball screw pair is predicted by the fractal theory combined with the test. The investigation leads to the following conclusions:

(1) The distribution curves of contact load and contact angle for nuts at different positions along the screw exhibit distinct variations, displaying complex nonlinear characteristics across the feed direction of the screw. The uneven contact load distribution in the middle position of the nut is superior to that at the screw ends. When the nut is located at the upper, middle, and lower end of the screw, the standard deviation of the contact load distribution is 78.38, 30.05, and 64.98, respectively. And the standard deviation of the contact angle distribution is 0.0337, 0.0130, and 0.0285, respectively.

(2) There is a similar evolutionary trend between contact load and axial load, as well as between contact angle and axial load. The unevenness of contact load distribution and contact angle distribution increases with the increase in axial load. When the axial load is 35,000 N/55,000 N/75,000 N, the standard deviation of the contact load distribution is 18.71/32.74/37.95 and the standard deviation of the contact angle distribution is 0.0096/0.0144/0.0191.

(3) The standard deviations of contact load distribution at different initial contact angles ($\alpha_0 = 45^\circ$, $\alpha_0 = 46^\circ$, and $\alpha_0 = 47^\circ$) are 32.74, 32.44, and 32.17, respectively, indicating a decreasing trend. The standard deviations of the contact angle distribution are constant, which is 0.0144.

(4) Due to the influence of guide rail geometric error and slide position, the contact stiffness of the double-drive ball screw pair shows complex nonlinearity as well.

Author Contributions: Methodology, formal analysis, validation, resources, writing original draft, Z.L.; methodology, formal analysis, writing, review, and editing, W.Z.; funding acquisition, writing, review, and editing, B.Q.; supervision, funding acquisition, C.C.; validation, formal analysis, J.G.; validation, formal analysis, D.L.; validation, resources, data processing, S.G. All authors have read and agreed to the published version of the manuscript.

Funding: This research was supported by the National Natural Science Foundation of China (No. 52305261), 2022 Horizontal Milling and Turning Compound Processing Center Project (No. TC220H060), China Postdoctoral Science Foundation (No. 2023M731278), and Chongqing Natural Science Foundation (No. CSTB2023NSCQ-MSX0473).

Data Availability Statement: The data that support the findings of this study are available from the authors upon reasonable request.

Acknowledgments: The authors would like to thank the research team members for their contributions to this work.

Conflicts of Interest: The authors declare no conflict of interest.

References

1. Huang, S.; Wang, S. Mechatronics and Control of a Long-Range Nanometer Positioning Servomechanism. *Mechatronics* **2009**, *19*, 14–28. [CrossRef]
2. Cheng, Q.; Qi, B.; Liu, Z.; Zhang, C.; Xue, D. An Accuracy Degradation Analysis of Ball Screw Mechanism Considering Time-Varying Motion and Loading Working Conditions. *Mech. Mach. Theory* **2019**, *134*, 1–23. [CrossRef]
3. Li, Y.; Mu, L.; Gao, P. Particle Swarm Optimization Fractional Slope Entropy: A New Time Series Complexity Indicator for Bearing Fault Diagnosis. *Fractal Fract.* **2022**, *6*, 345. [CrossRef]
4. Liu, C.; Zhao, C.; Meng, X.; Wen, B. Static Load Distribution Analysis of Ball Screws with Nut Position Variation. *Mech. Mach. Theory* **2020**, *151*, 103893. [CrossRef]
5. Qi, B.; Zhao, J.; Chen, C.; Song, X.; Jiang, H. Accuracy Decay Mechanism of Ball Screw in CNC Machine Tools for Mixed Sliding-Rolling Motion under Non-Constant Operating Conditions. *Int. J. Adv. Manuf. Technol.* **2023**, *124*, 4349–4363. [CrossRef]
6. Li, Y.; Tang, B.; Geng, B.; Jiao, S. Fractional Order Fuzzy Dispersion Entropy and Its Application in Bearing Fault Diagnosis. *Fractal Fract.* **2022**, *6*, 544. [CrossRef]
7. Meng, J.; Du, X.; Li, Y.; Chen, P.; Xia, F.; Wan, L. A Multiscale Accuracy Degradation Prediction Method of Planetary Roller Screw Mechanism Based on Fractal Theory Considering Thread Surface Roughness. *Fractal Fract.* **2021**, *5*, 237. [CrossRef]
8. Nastac, S. On Vibration Joint Time-Frequency Investigations of CNC Milling Machines for Tool Trajectory Task Conformity Estimation. *Shock Vib.* **2018**, *2018*, 7375057. [CrossRef]
9. Tang, H.; Duan, J.; Zhao, Q. A Systematic Approach on Analyzing the Relationship between Straightness & Angular Errors and Guideway Surface in Precise Linear Stage. *Int. J. Mach. Tools Manuf.* **2017**, *120*, 12–19.
10. Wang, Z.; Wang, D.; Wu, Y.; Dong, H.; Yu, S. Error Calibration of Controlled Rotary Pairs in Five-Axis Machining Centers Based on the Mechanism Model and Kinematic Invariants. *Int. J. Mach. Tools Manuf.* **2017**, *120*, 1–11. [CrossRef]
11. Qiao, Y.; Chen, Y.; Yang, J.; Chen, B. A Five-Axis Geometric Errors Calibration Model Based on the Common Perpendicular Line (CPL) Transformation Using the Product of Exponentials (POE) Formula. *Int. J. Mach. Tools Manuf.* **2017**, *118–119*, 49–60. [CrossRef]
12. Huang, N.; Jin, Y.; Bi, Q.; Wang, Y. Integrated Post-Processor for 5-Axis Machine Tools with Geometric Errors Compensation. *Int. J. Mach. Tools Manuf.* **2015**, *94*, 65–73. [CrossRef]
13. Feng, W.L.; Yao, X.D.; Azamat, A.; Yang, J.G. Straightness Error Compensation for Large CNC Gantry Type Milling Centers Based on B-Spline Curves Modeling. *Int. J. Mach. Tools Manuf.* **2015**, *88*, 165–174. [CrossRef]
14. Niu, P.; Cheng, Q.; Zhang, T.; Yang, C.; Zhang, Z.; Liu, Z. Hyperstatic Mechanics Analysis of Guideway Assembly and Motion Errors Prediction Method under Thread Friction Coefficient Uncertainties. *Tribol. Int.* **2023**, *180*, 108275. [CrossRef]
15. Hwang, J.; Park, C.; Gao, W.; Kim, S. A Three-Probe System for Measuring the Parallelism and Straightness of a Pair of Rails for Ultra-Precision Guideways. *Int. J. Mach. Tools Manuf.* **2007**, *47*, 1053–1058. [CrossRef]
16. Feng, G.; Pan, Y. Investigation of Ball Screw Preload Variation Based on Dynamic Modeling of a Preload Adjustable Feed-Drive System and Spectrum Analysis of Ball-Nuts Sensed Vibration Signals. *Int. J. Mach. Tools Manuf.* **2012**, *52*, 85–96. [CrossRef]
17. Ekinci, T.; Mayer, J. Relationships between Straightness and Angular Kinematic Errors in Machines. *Int. J. Mach. Tools Manuf.* **2007**, *47*, 1997–2004. [CrossRef]
18. Zha, J.; Xue, F.; Chen, Y. Straightness Error Modeling and Compensation for Gantry Type Open Hydrostatic Guideways in Grinding Machine. *Int. J. Mach. Tools Manuf.* **2017**, *112*, 1–6. [CrossRef]
19. Mei, X.; Tsutsumi, M.; Tao, T.; Sun, N. Study on the Load Distribution of Ball Screws with Errors. *Mech. Mach. Theory* **2003**, *38*, 1257–1269. [CrossRef]
20. Wei, C.; Lin, J. Kinematic Analysis of the Ball Screw Mechanism Considering Variable Contact Angles and Elastic Deformations. *J. Mech. Des.* **2003**, *125*, 717–733. [CrossRef]
21. Gu, J.; Zhang, Y. Dynamic Analysis of a Ball Screw Feed System with Time-Varying and Piecewise-Nonlinear Stiffness. *Proc. Inst. Mech. Eng. Part C J. Mech. Eng. Sci.* **2019**, *233*, 6503–6518. [CrossRef]
22. Lin, M.; Ravani, B.; Velinsky, S. Kinematics of the Ball Screw Mechanism. *J. Mech. Des.* **1994**, *116*, 849–855. [CrossRef]
23. Hu, J.; Wang, M.; Zan, T. The Kinematics of Ball-Screw Mechanisms via the Slide–Roll Ratio. *Mech. Mach. Theory* **2014**, *79*, 158–172. [CrossRef]
24. Huang, H.; Tsai, M.; Huang, Y. Modeling and Elastic Deformation Compensation of Flexural Feed Drive System. *Int. J. Mach. Tools Manuf.* **2018**, *132*, 96–112. [CrossRef]
25. Zhou, C.; Feng, H.; Chen, Z.; Ou, Y. Correlation between Preload and No-Load Drag Torque of Ball Screws. *Int. J. Mach. Tools Manuf.* **2016**, *102*, 35–40. [CrossRef]
26. Liu, J.; Feng, H.; Zhou, C. Static Load Distribution and Axial Static Contact Stiffness of a Preloaded Double-Nut Ball Screw Considering Geometric Errors. *Mech. Mach. Theory* **2022**, *167*, 104460. [CrossRef]

27. Zhao, J.; Lin, M.; Song, X.; Guo, Q. Investigation of Load Distribution and Deformations for Ball Screws with the Effects of Turning Torque and Geometric Errors. *Mech. Mach. Theory* **2019**, *141*, 95–116. [CrossRef]
28. *ISO 230-1:2012*; Test Code for Machine Tools—Part 1: Geometric Accuracy of Machines Operating under No-Load or Quasi-static Conditions. ISO: Geneva, Switzerland, 2012.
29. Lin, M.; Velinsky, S.; Ravani, B. Design of the Ball Screw Mechanism for Optimal Efficiency. *J. Mech. Des.* **1994**, *116*, 856–861. [CrossRef]
30. Wei, C.; Lin, J.; Horng, J. Analysis of a Ball Screw with a Preload and Lubrication. *Tribol. Int.* **2009**, *42*, 1816–1831. [CrossRef]
31. Zhao, H.; Wu, Q. Application Study of Fractal Theory in Mechanical Transmission. *Chin. J. Mech. Eng.* **2016**, *29*, 871–879. [CrossRef]
32. Zhao, Y.; Wu, H.; Liu, Z.; Cheng, Q.; Yang, C. A Novel Nonlinear Contact Stiffness Model of Concrete–Steel Joint Based on the Fractal Contact Theory. *Nonlinear Dyn.* **2018**, *94*, 151–164. [CrossRef]
33. Liu, J.; Ma, C.; Wang, S. Precision Loss Modeling Method of Ball Screw Pair. *Mech. Syst. Signal Process.* **2020**, *135*, 106397. [CrossRef]